ADVANCED MATERIALS

Supporting Information

for *Adv. Mater.*, DOI: 10.1002/adma.201705197

Direct Visualization of the Reversible O^{2-}/O^{-} Redox Process in Li-Rich Cathode Materials

Xiang Li, Yu Qiao, Shaohua Guo, Zhenming Xu, Hong Zhu, Xiaoyu Zhang, Yang Yuan, Ping He,* Masayoshi Ishida, and Haoshen Zhou**

Supporting Information

Direct Visualization of Reversible O^{2-}/O^{-} Redox Process in Li-Rich Cathode Materials

Xiang Li, Yu Qiao, Shaohua Guo, Zhenming Xu, Hong Zhu, Xiaoyu Zhang, Yang Yuan, Ping He,* Masayoshi Ishida, and Haoshen Zhou**

Experimental Section

Synthesis of $Li_{1.2}Ni_{0.2}Mn_{0.6}O_2$:

Co-precipitation method was used to prepare the precursor which can be found in our previous study.[1] Reagents included ammonium hydroxide (AR, Nanjing Chemical Reagent Co., Ltd.), nickel sulfate hexahydrate (AR, Enox), manganese sulfate monohydrate (AR, Xilong Chemical Industry Co., Ltd.), and sodium hydroxide (AR, Nanjing Chemical Reagent Co., Ltd.). Briefly, the deoxidized aqueous solution of metal sulfates were slowly dropped into 1M NH_3(aq) controlled by peristaltic pumps, with stable PH value maintained by NaOH(aq). After filtering and washing adequately, the black precursor was dried in a drying oven at 80 ^oC for 10 h.

As-prepared precursor Ni_xMn_yOH (x:y=1:3) was mixed with 3 wt% excess $LiOH{\cdot}H_2O$ powders thoroughly, then, $Li_{1.2}Ni_{0.2}Mn_{0.6}O_2$ was obtained by calcining the mixture in the furnace at 750 ^oC for 12 h in air.

Characterizations:

The structure of $Li_{1.2}Ni_{0.2}Mn_{0.6}O_2$ was identified by powder XRD (Ultima III, Rigaku Corporation) radiation from Cu Kα (λ = 1.5406 Å). The data were collected between diffraction angles (2θ) from 10^o to 80^o at a scan rate of 2^o per min. Rietveld refinements of the XRD pattern obtained by GSAS + EXPGUI suite. The morphologies of the materials were procured by SEM (JSM-7000F). In-situ Raman spectra of the materials were obtained using a homemade mould and JASCO microscope spectrometer (NRS-1000DT).

Electrochemical tests:

2032 coin-type cells were used for electrochemical measurements. The electrodes consisted of active material, acetylene black, and polytetrafluoroethene (PTFE, 12 wt.%) binder with the weight ratio of 85:10:5. 1 M $LiClO_4$ in propylene carbonate (PC) was prepared as the electrolyte. LAND 2001A Battery Testing Systems (Wuhan LAND electronics Co., Ltd, P.R. China) were employed for galvanostatic testing.

In-situ Raman observation:

A detailed description of the modified in-situ Raman cell (Hohsen Corp., Osaka, Japan) for the Li-ion battery employed in this study can be found in our previous study.[2] In detail, a thin quartz window (thickness, 0.5 mm) has been fixed on the top of the cell as a sight window. In order to collect shell-isolated nanoparticle-enhanced Raman (SHINER) signal, gold nanoparticles (NPs) approximately 40 nm in diameter with a SiO_2 coating shell (~5 nm) were synthesized as in previous reports.[3] The washed and dried Au@SiO_2 NPs were dripped onto the specific cathode surface and vacuum dried before assembly. The cathode was assembled at the bottom of the cell with the active material-face upward. On the top of the cathode, 50-100 μL of electrolyte was homogeneously dropped onto the glassy fiber filter separator (GF/A, Whatman). As a standard two-electrode configuration cell, lithium foil (thickness, 0.4 mm) was assembled at the top as the reference and counter electrode. Note that, a small hole was punched on the center of both the separator and Li foil, through which the laser and Raman signals can fluidly cross. The cell was assembled in an argon-filled glovebox.

The Raman spectra were recorded using a JASCO microscope spectrometer (NRS-1000DT). The excitation light of an air-cooled He−Ne laser at 632.8 nm wavelength was focused on the electrode surface through a 50×long working distance lens (Olympus America Inc.). The confocal slit was adjusted to be 4.0 μm to minimize the band broadening effect due to the contribution of non-confocal signal. The scattered light was collected in a backscattering geometry along the same optical path as the pumping laser. The power of laser beam delivered to the electrode surface was roughly 10% of the maximum 30 mW laser intensity, unless specified, to avoid degradation to the products and/or cathode. The Raman spectrum acquisition time varied from 600~800 s with 2 accumulations. At least 3 different places on the electrode surface at each cathode plate were checked to ensure the Raman spectra were credible and reproducible. The spectral resolution of the Raman spectra in the study was ca. 1.0 cm^{-1}.

For the in-situ Raman test, the electrochemical experiments were carried out under the control of a potentiostat (Potentiostat/Galvanostat PGSTAT30, Autolab Co. Ltd., Netherlands) at room temperature. The current and potential outputs from the potentiostat were recorded by a multifunction data acquisition module/amplifier (PGSTAT30 Differential Electrometer, Autolab), which was controlled by General Purpose Electrochemical Software (GPES). Typically, the galvanostatic control was carried out at a current density of 5 mA g^{-1}. Before characterization, the cell was kept on an open circuit for 10 h. The OCP was approximately 3.0 V in most cases in the study. All of the potentials in this study were referenced to Li/Li^+.

DFT Calculation:

All calculations were carried out by using the projector augmented wave (PAW) method[4] in the framework of DFT[5], as implemented in the Vienna *ab-initio* Simulation Package (VASP). The generalized gradient approximation (GGA)[6] and Perdew–Burke–Ernzerhof (PBE) exchange functional[5] was used. The periodic boundary condition approach was used. The plane-wave energy cutoff was set to 450 eV. The Monkhorst–Pack method[7] with 1×4×1 *k*-points mesh was employed for the Brillouin zone sampling of the structural relaxations of $Li_{1.2-x}Ni_{0.2}Mn_{0.6}O_2$. The convergence criterions of the energy and force were 10^{-4} eV/atom and 0.05 eV $Å^{-1}$, respectively.

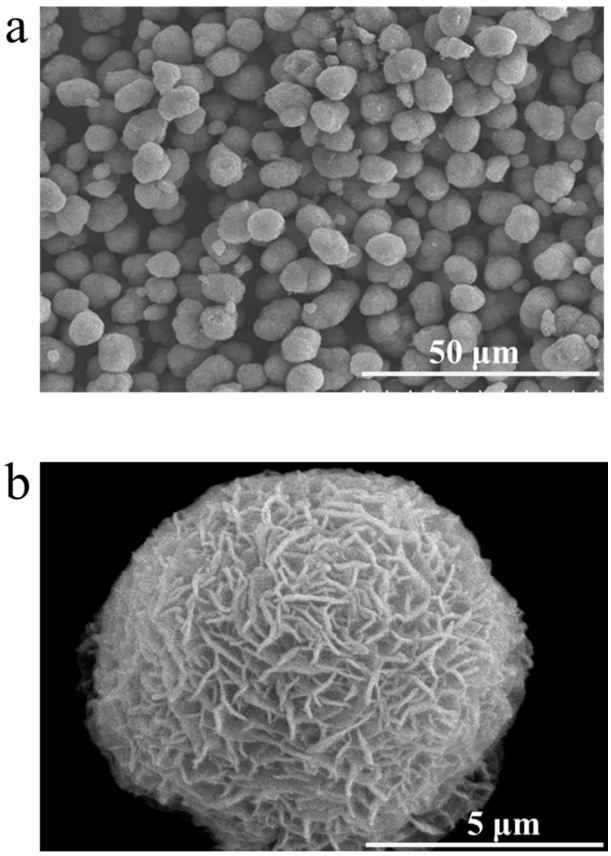

Figure S1. SEM images of precursor in different magnification. × 1.0 k (a) and × 10.0 k (b).

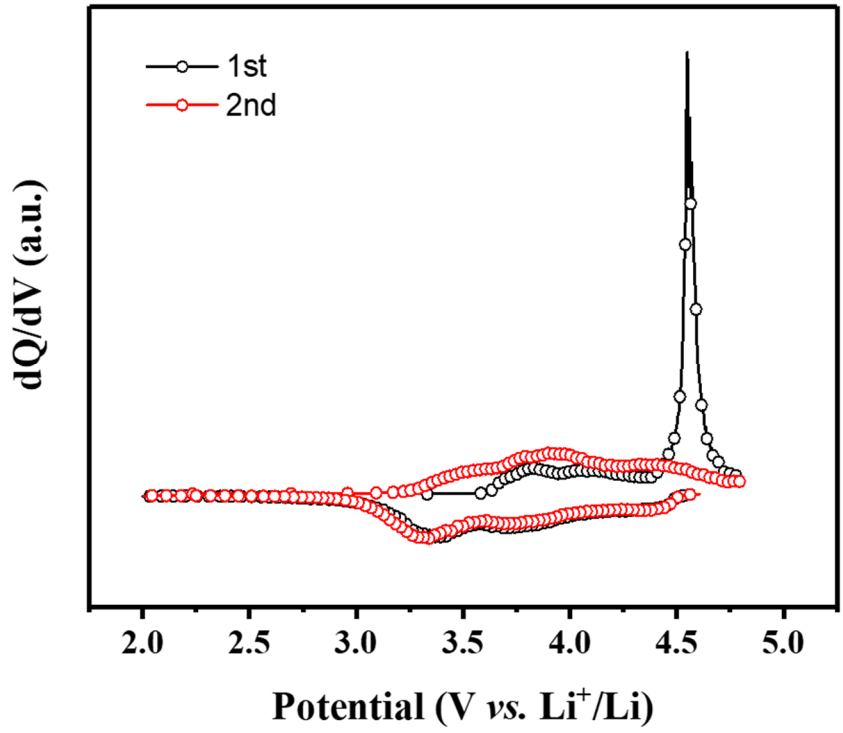

Figure S2. dQ/dV curves for initial two cycles of $Li_{1.2}Ni_{0.2}Mn_{0.6}O_2$ at 5 mA g^{-1}. The black dotted line represents the first cycle and the red dotted line represents the second cycle.

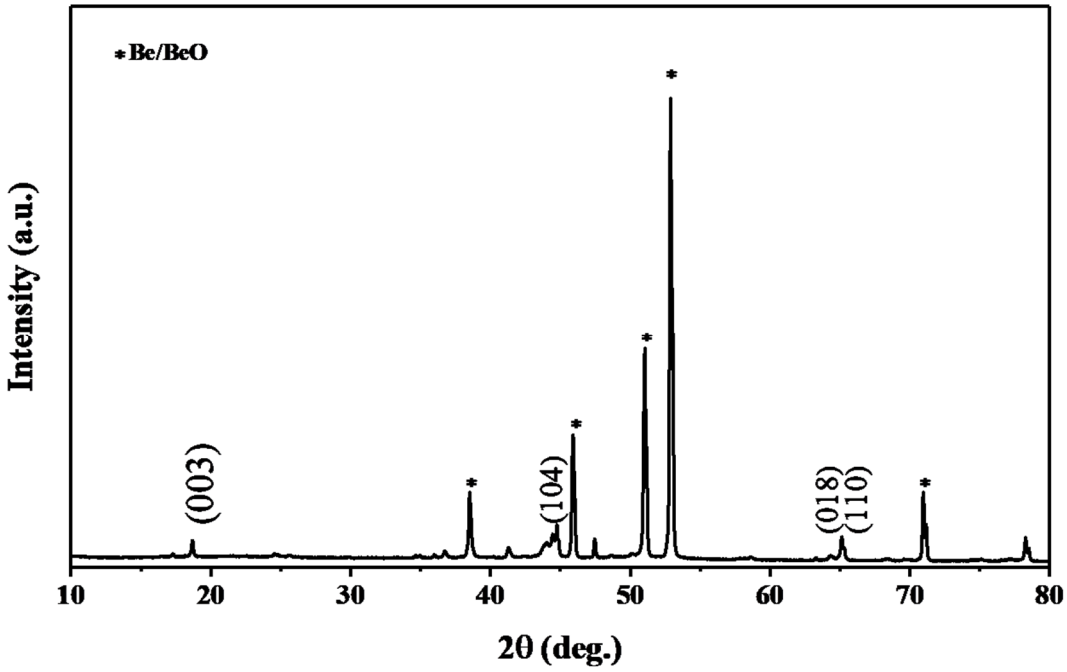

Figure S3. XRD pattern of $Li_{1.2}Ni_{0.2}Mn_{0.6}O_2$ in the in-situ mold. Peaks marked by * belong to Be/BeO.

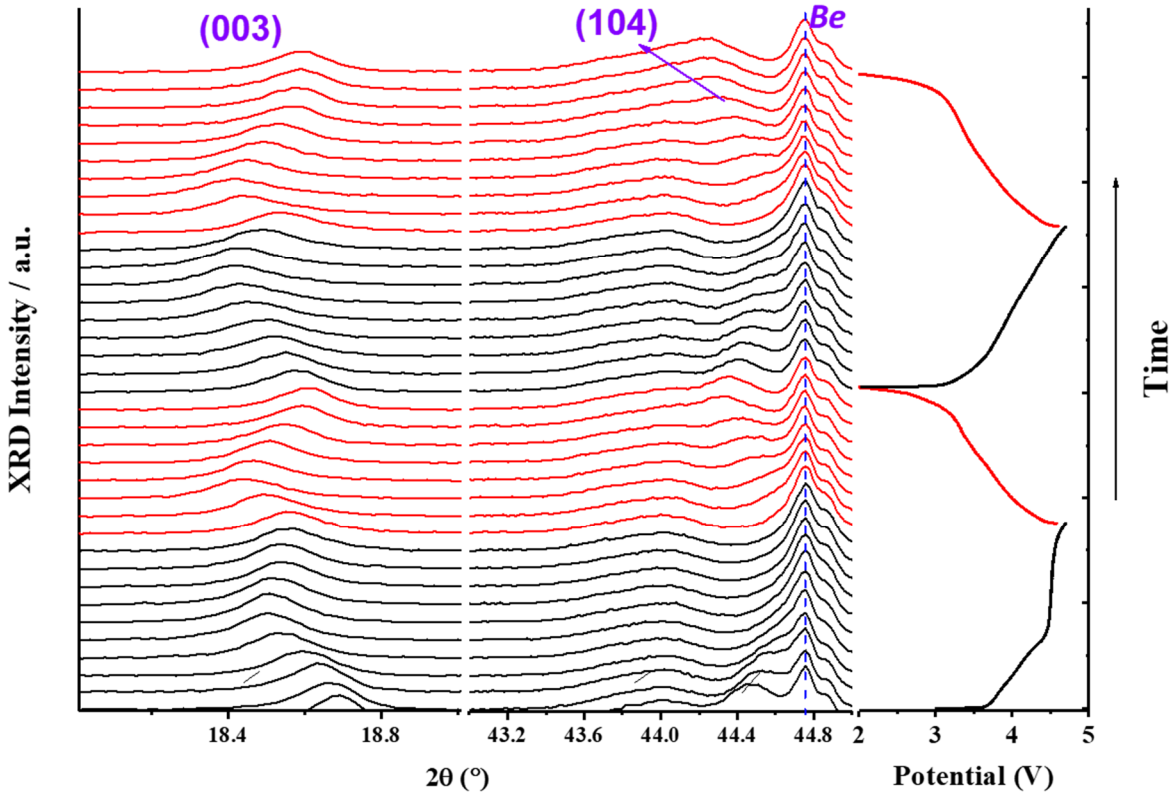

Figure S4. The in-situ XRD patterns of the evolution for the peaks (003) and (104), combined with corresponding electrochemical testing result during the first two cycles for the material $Li_{1.2}Ni_{0.2}Mn_{0.6}O_2$. The black line represents the charge process and the red line represents the discharge process.

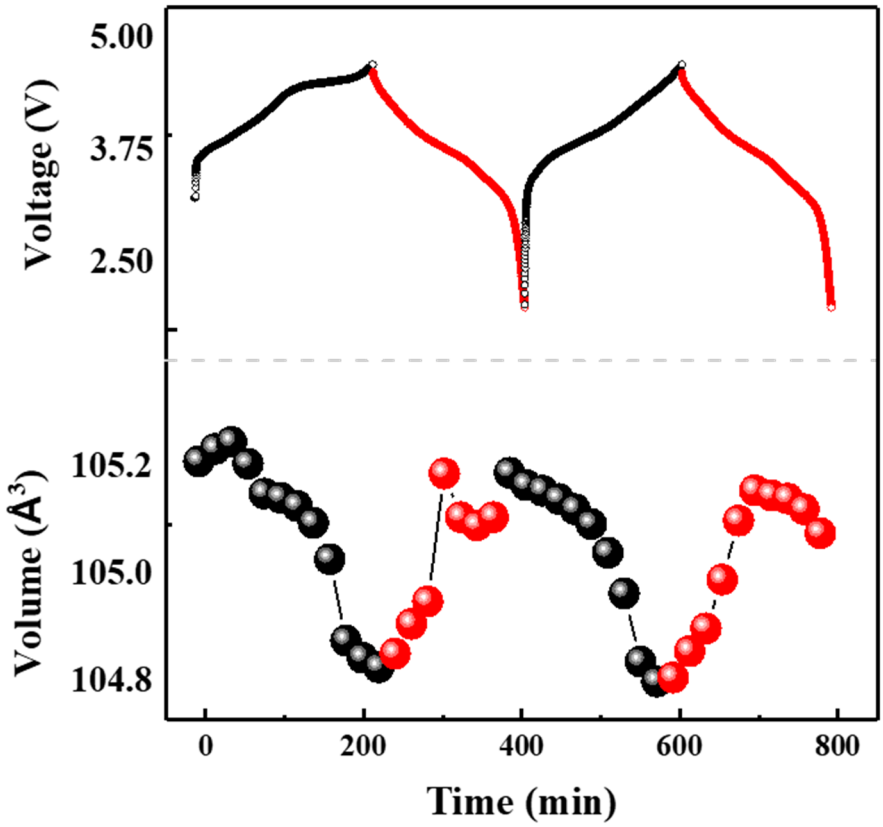

Figure S5. The charging and discharging curves of the first two cycles and changes of the Rietveld refined unit cell volume for $Li_{1.2}Ni_{0.2}Mn_{0.6}O_2$. The black and red colors represent charging and discharging process respectively.

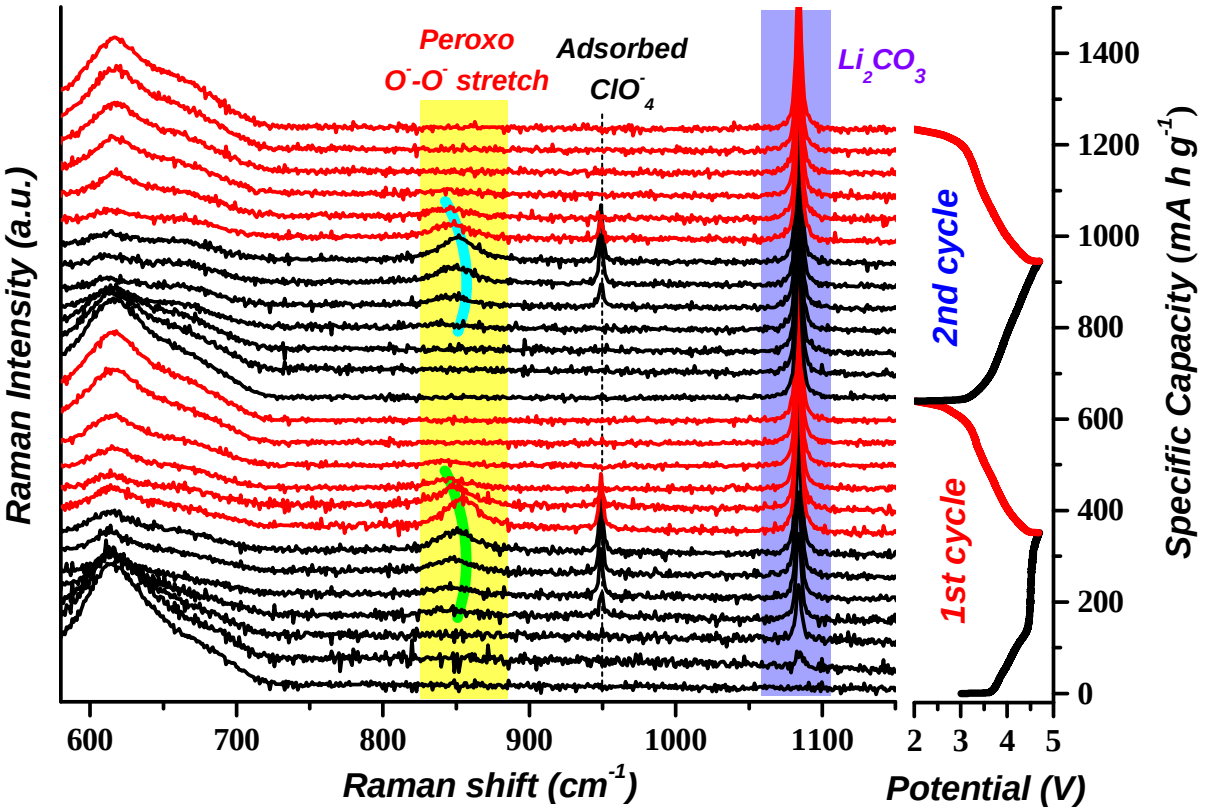

Figure S6. In situ Raman spectra (SERS-signal) recorded during initial two galvanostatic cycles with extended Raman shift range, which includes Li_2CO_3-related peak (~1080 cm^{-1}) as comparison. Note that, the formation of carbonate species would be rationally ascribed to the parasitic reaction between electrolyte and other active oxygen-related species (superoxide anion radical and/or oxygen), which release from the lattice ($Li_{1.2}Ni_{0.2}Mn_{0.6}O_2$) upon charging (irreversible oxygen loss). This parasitic accumulation of Li_2CO_3 is also well coincide with previous reports.[8]

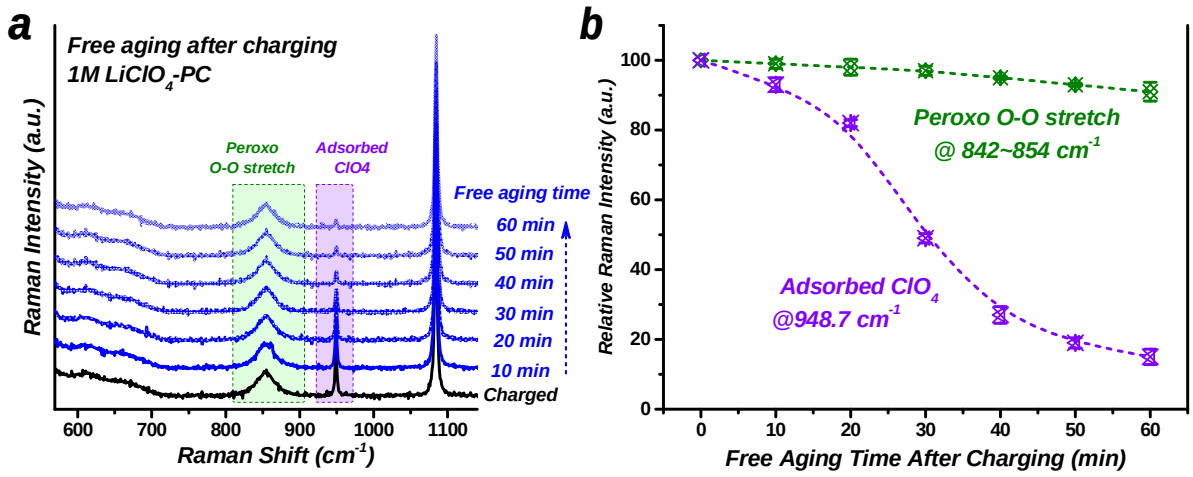

Figure S7. Aging time test of O-O peak and ClO_4^- peak after charging. a) Changes of Raman intensity with aging time and b) relative Raman intensity with aging time.

The change of unique adsorbed ClO_4^- peak is a function of potential. There is no relationship between O-O peak and adsorbed ClO_4^- peak, which can be confirmed by aging test. As shown in **Figure S7**, we stopped the procedure and let the cell free at the end of charging process. The variation of Raman intensity of O-O peak and ClO_4^- peak are obvious in **Figure S7a** and more distinct in **Figure S7b**. The intensity of ClO_4^- peak decreases dramatically as a function of aging time, resulting from the essential reason-decrease of the potential. The intensity of O-O peak, however, basically remain unchanged with aging time.

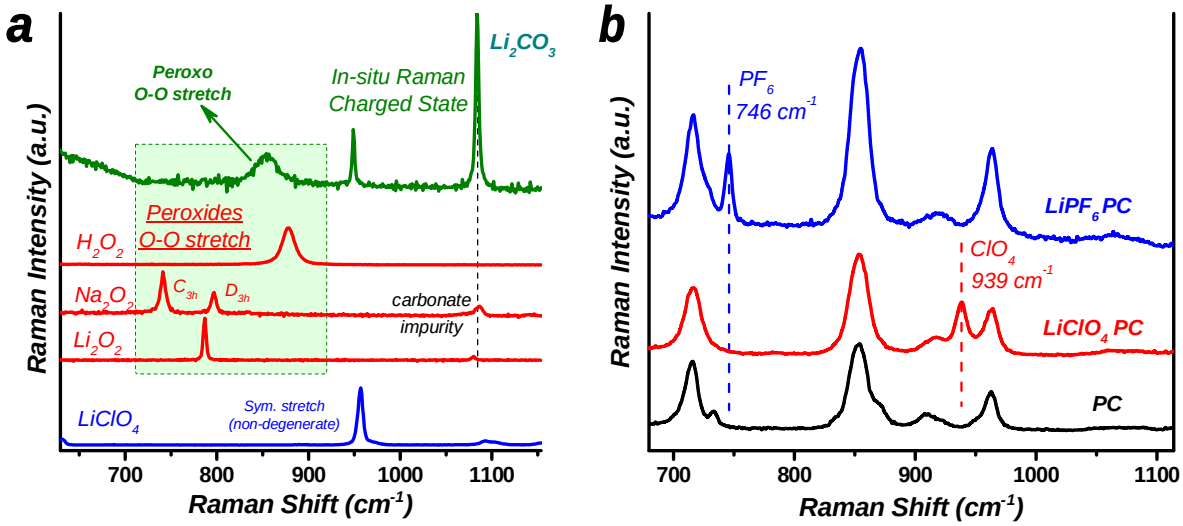

Figure S8. Raman peaks of standard materials of a) $LiClO_4$, Li_2O_2, Na_2O_2, H_2O_2, and charged state electrode and b) PC, electrolyte of 1M $LiClO_4$ in PC and electrolyte of 1M $LiPF_6$ in PC.

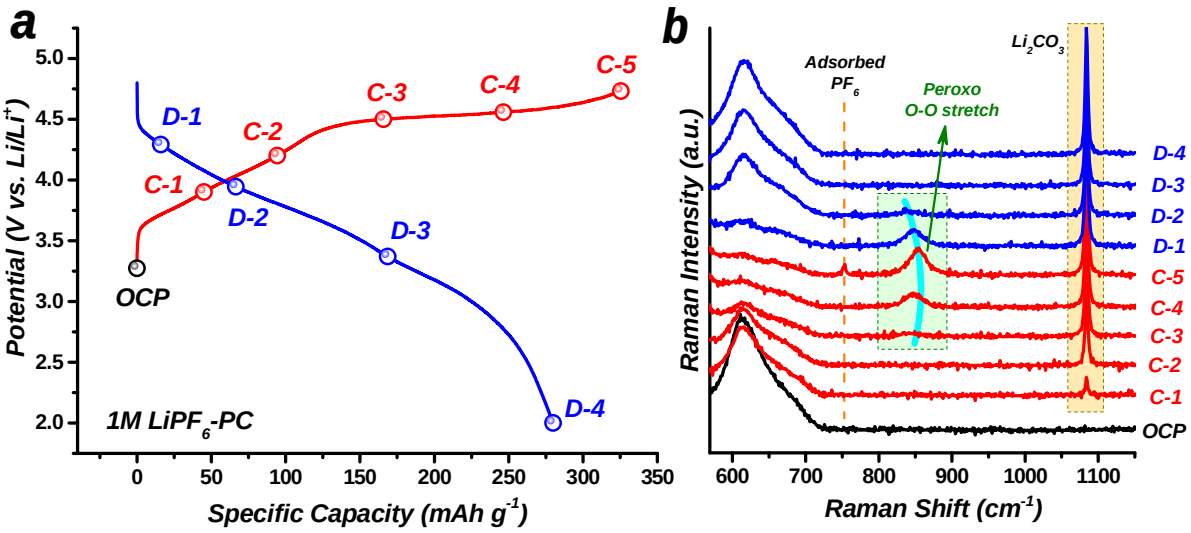

Figure S9. a) Typical charge-discharge profiles between 2.0 and 4.7 V with electrolyte of 1M $LiPF_6$ in PC at 10 mA g^{-1} and b) in situ Raman spectra recorded during initial galvanostatic cycle.

The phenomenon of adsorbed ClO_4^- peak coupled with peroxide species in **Figure 3**, however, made a confusion because it seems ClO_4^- may be additional source for O-O dimers. We have confirmed that the adsorbed ClO_4^- peak is potential-dependent and has no relationship with O-O bonding. Furthermore, we did the similar experiment in $LiPF_6$ (1M in PC), as shown in **Figure S9.** A new peak (O-O) at ~ 850 cm^{-1} emerges and increases during the 4.5 V-related charging plateau, and gradually disappears with the subsequent discharge process, similar to the phenomenon in $LiClO_4$-salt electrolyte. Another similar phenomenon is that a new peak at ~ 1080 cm^{-1} emerges and increases during the charging process and without decrease even in discharging process, which can be assigned to Li_2CO_3. Moreover, the adsorbed PF_6^- peak appears until the end of charging process, which is also potential-dependent.

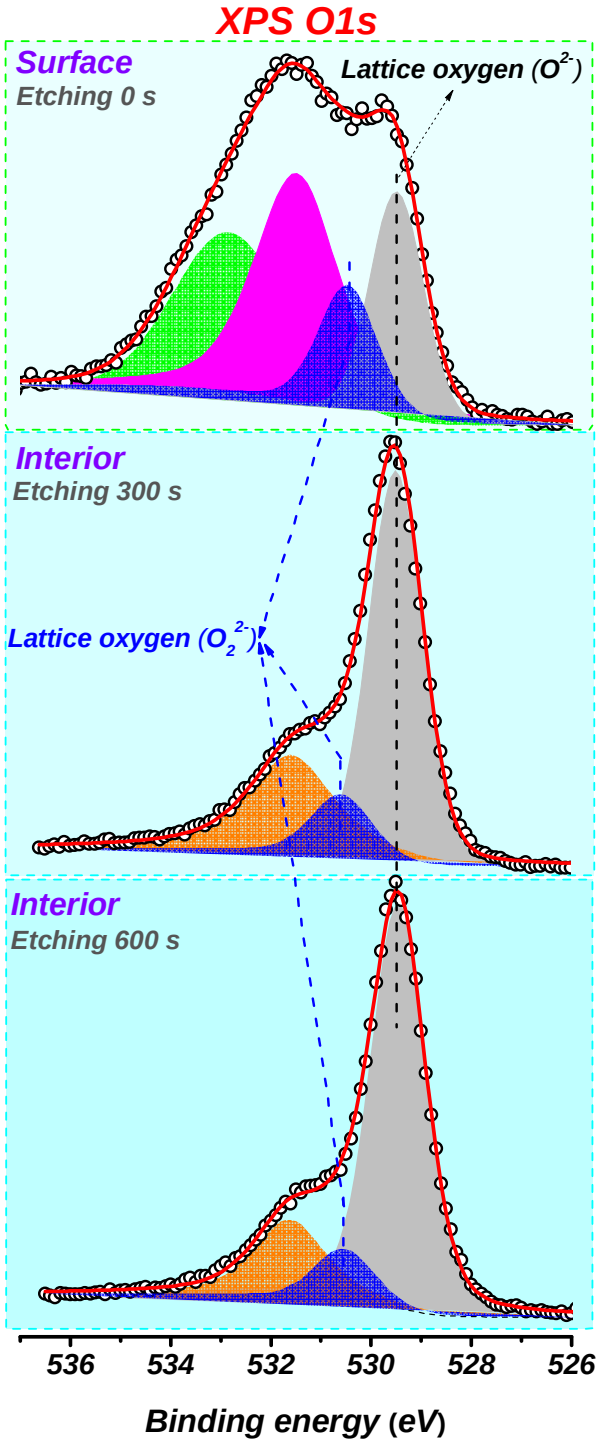

Figure S10: Oxygen 1s XPS spectra of the charged $Li_{1.2}Ni_{0.2}Mn_{0.6}O_2$ electrode at 4.7 V, which were collected in the surface, after Ar^+ etching 300 s and 600 s. The grey, blue, green, and pink areas represent the lattice oxygen (O^{2-}), lattice oxygen (O_2^{2-}), surface deposited species and electrolyte oxidation, respectivily. The brown area may be caused by the oxygen deficiencies.

To understand the formation of O-O dimers in the bulk or in the surface, depth analysis was employd by the X-ray photoelectron spectroscopy (XPS). XPS spectra were obtained from the

surface of the charged electrode at 4.7 V and that after different times of Ar^+-sputtering. Before etching by argon sputtering, peaks were observed at ~ 529.5 eV, 530.5 eV, 531.5 eV, and 532.8 eV which are assigned to lattice oxygen (O^{2-}), lattice oxygen (O_2^{2-}), surface deposited species and electrolyte oxidation, respectivily. The peaks and their positions are consistent well with Tarascon and co-authours' works.[9] After argon sputtering, the peak assigned to electrolyte oxidation disappears. The spectrum after etching 300 s is as same as that after etching 600 s, meaning the internal structure was obtained after sputtering 300 s. Obviously, the peak located at 530.5 eV (bule area) can be clearly seen after sputtering, which is assigned to peroxy oxygen dimers (the brown area may be caused by the oxygen deficiencies[10]). Herein, the peroxo oxygen dimers exist both in surface and in internal. Note that, the composition of the electrode may change after sputtering, however, the result can be reliable after some concessions we made in etching time and pattern quality.[11]

DFT calculation model:

Lithium honeycomb ordering is common in many lithium-excess compounds, corresponding to the additional superlattice peaks in XRD pattern. However, the honeycomb structure is short-range order because of the non-uniform distribution of the cations (Li, Ni, Mn) in transition metal layers.[12] It means that there exist mixed ordering types such as honeycomb-type and straight-type in transition metal layers.[12, 13] Here, we present the detailed reasons why we chose the straight-type model for first principle calculation, after considering the several configurations in transition-metal layers.

In our calculations, the honeycomb type ordering of excess lithium atoms was studied. Considering the balance between computing workloads and the accuracy of calculation model, a lithium honeycomb type ordering structure with the composition of $Li_{1.22}Ni_{0.22}Mn_{0.56}O_2$ is bulit, as shown in Figure S11. Although the composition of $Li_{1.22}Ni_{0.22}Mn_{0.56}O_2$ is slightly different from our experimental $Li_{1.2}Ni_{0.2}Mn_{0.6}O_2$, it can well represent the local honeycomb ordering of lithium atoms in $Li_{1.2}Ni_{0.2}Mn_{0.6}O_2$. Thus, we investigated the peroxo bond formation in the fully delithiated $Li_{1.22}Ni_{0.22}Mn_{0.56}O_2$ compound, whose honeycomb ordered Li atom in transition metal layer are fully extracted to represent the charging final structure. The corresponding energy barrier of the peroxy bond formation in it is depicted in Figure S12. It can be seen that forming a peroxo bond with the O-O bond length less than 1.46 Å (a typical value of peroxy bond)[14] in this lithium honeycomb type structure is endothermic, more than 1 eV ~96 KJ/mol, and needs to overcome a very large energy barrier of 1.44 eV. Such high energy barriers of peroxy bond formation also can be found in Li_2MnO_3 compounds, 0.6-1 eV.[14] Generally, the thermal vibration energy of an atom is KT, ~0.026 eV at 300K, which is far less than the energy barrier for the peroxy bond formation, so the possibility of forming peroxy bonds in the lithium-excess compounds with

the local lithium honeycomb type structure in $Li_{1.2}Ni_{0.2}Mn_{0.6}O_2$ during the charging and discharging process at room environment is extremely low.

We calculated the relative energy of some other $Li_{1.2}Ni_{0.2}Mn_{0.6}O_2$ structures with different lithium atom orderings in transition metal layer, as shown in Figure S13. Refer to the case 1 with dispersive lithium atom orderings, the relative energy of case 5 structure with local lithium straight-type tripolymers is 35.45 meV/atom, slightly more than the room temperature atom thermal vibration energy ~26 meV/atom, but far less than the high temperature atom thermal vibration energy ~101.67 meV/atom at the synthesizing temperature of 900 ^{o}C. Therefore, the lithium straight-type tripolymers in some local areas of our experimental case are highly possible, and they are also observed in some other lithium-excess compounds, such as $Li_{1.15}Ni_{0.47}Sb_{0.38}O_2$.[13]

In addition, we have investigated the peroxo bond formation in these $Li_{1.2}Ni_{0.2}Mn_{0.6}O_2$ structures in Figure S13. Similarly, forming peroxy bonds in these structures are difficult with larger energy barriers compared to straight-type tripolymer structure. While the local lithium straight-type tripolymers model (Figure S14) is beneficial for the formation of peroxy bonds without energy barrier, which is a spontaneous exothermic process. Therefore, the local lithium straight-type tripolymers model in DFT calculations can explain the formation and evolution of peroxy bonds during the charging and discharging process of our experiment.

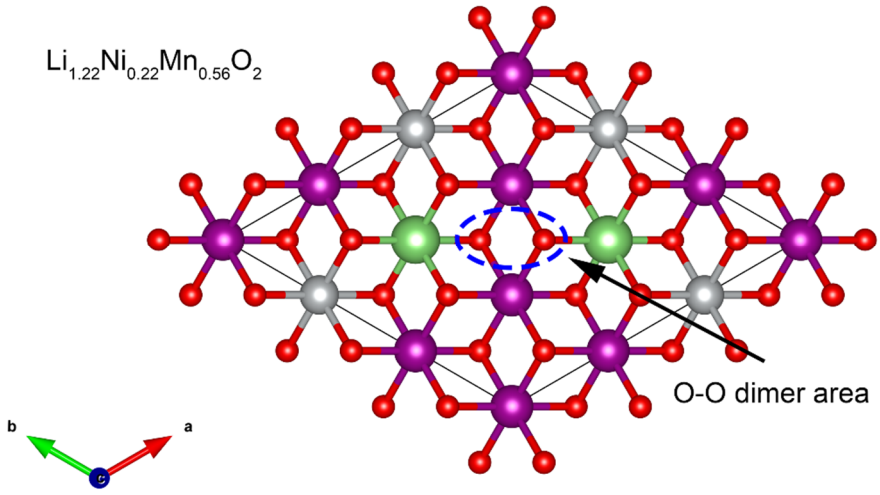

Figure S11. Honeycomb ordering of Li atoms in the transition metal layer of lithium-excess $Li_{1.22}Ni_{0.22}Mn_{0.56}O_2$ compound. The white, purple, green and red spheres represent Li, Mn, Ni and O atoms, respectively.

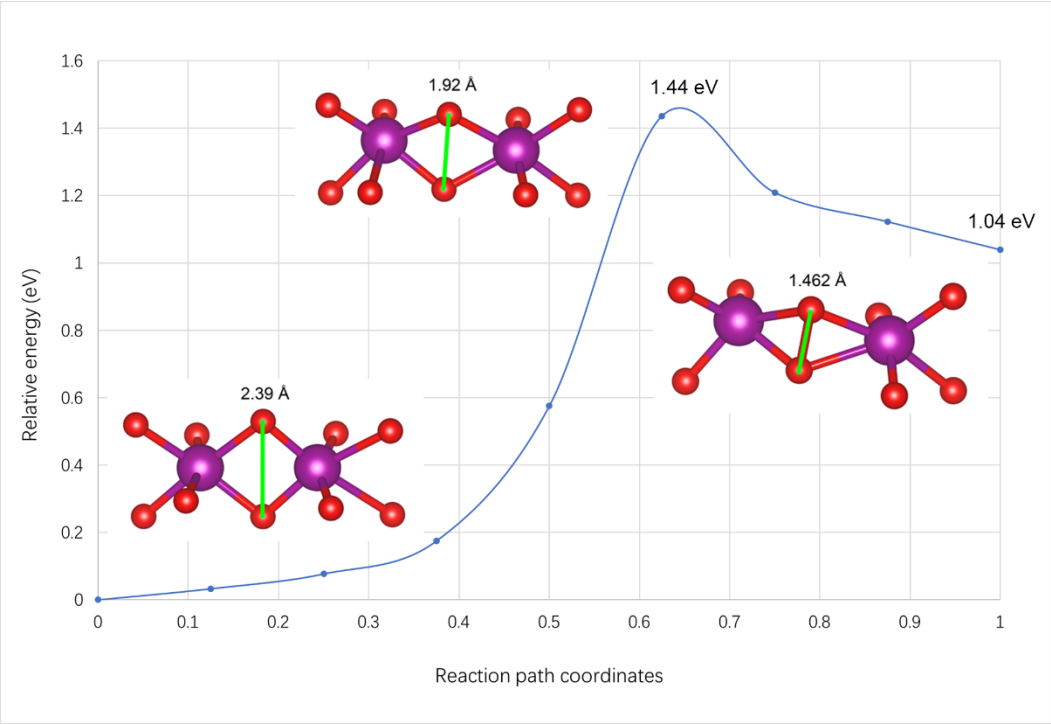

Figure S12. Energy barrier (eV) of the peroxy bond formation in fully delithiated $Li_{1.22}Ni_{0.22}Mn_{0.56}O_2$ compound with honeycomb orderings of Li atoms at the end of charging (Insets are the local structures for peroxo bond formation, including initial structure, transition state structure and final structure).

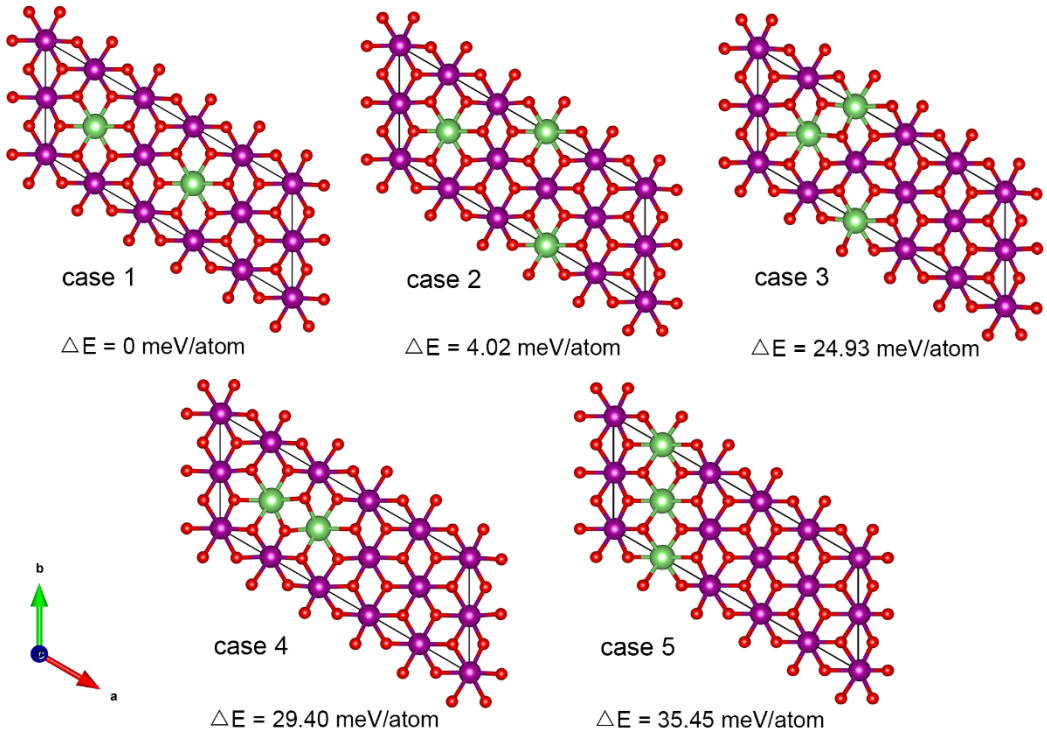

Figure S13. The relative energy (in meV/atom, and referred to case 1) of $Li_{1.2}Ni_{0.2}Mn_{0.6}O_2$ compounds with different lithium atom orderings in the transition metal layer.

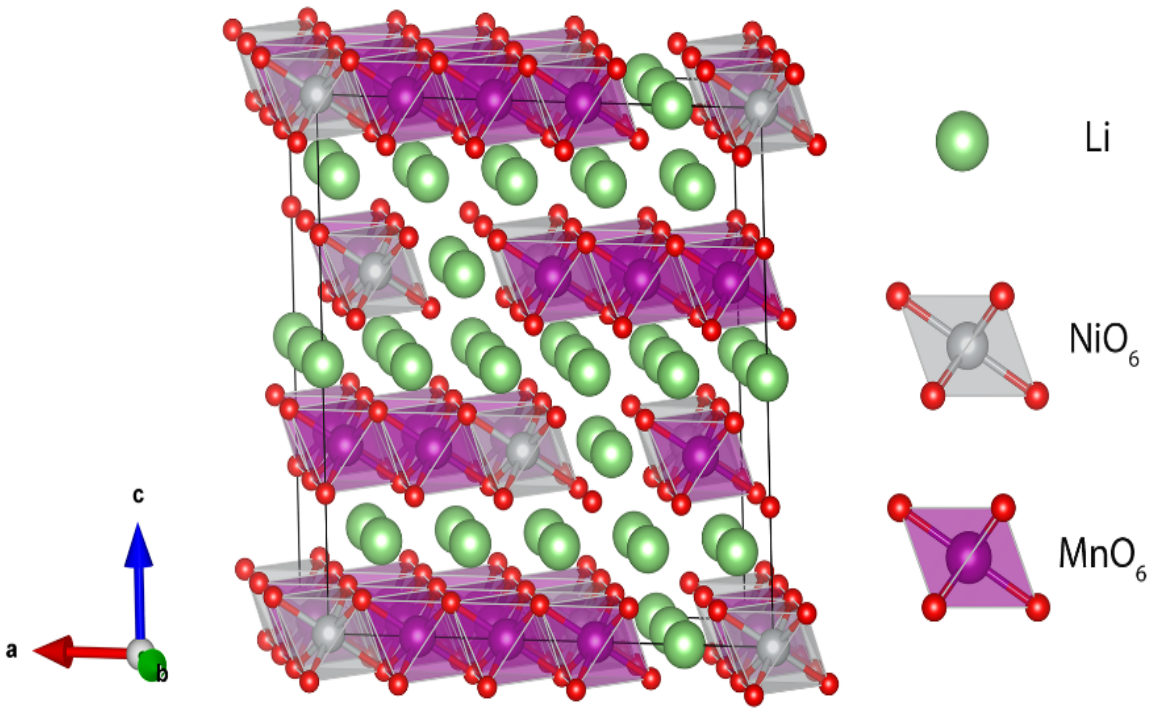

Figure S14. The optimized crystal structure of $Li_{1.2}Ni_{0.2}Mn_{0.6}O_2$. The green, silver, purple and red spheres represent Li, Ni, Mn and O atoms, respectively.

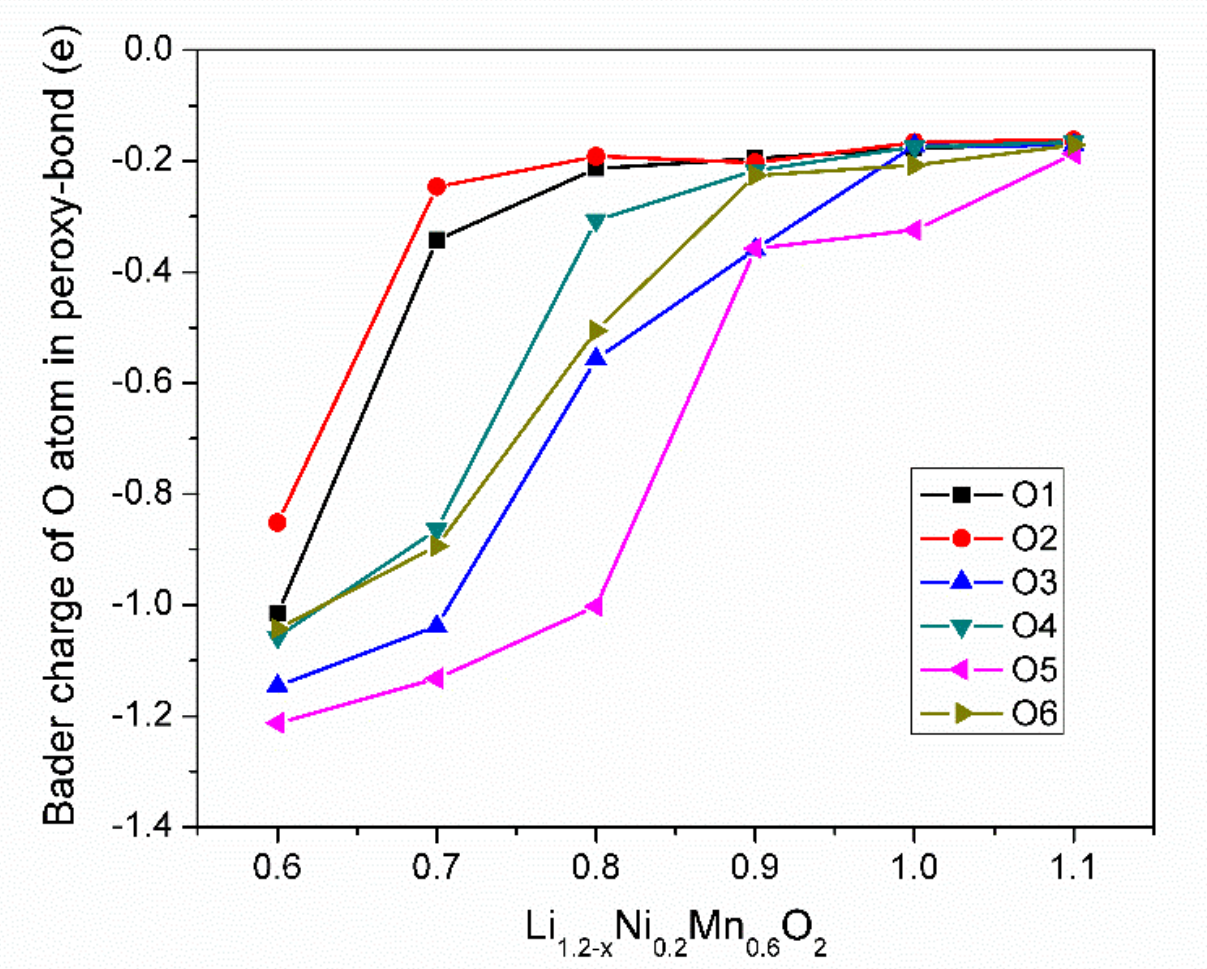

Figure S15. O atomic Bader charge (*e*) of the peroxo O-O bonds of the $Li_{1.2-x}Ni_{0.2}Mn_{0.6}O_2$ systems (x = 0.6, 0.7, 0.8, 0.9, 1.0 and 1.1) during the charging and discharging processes

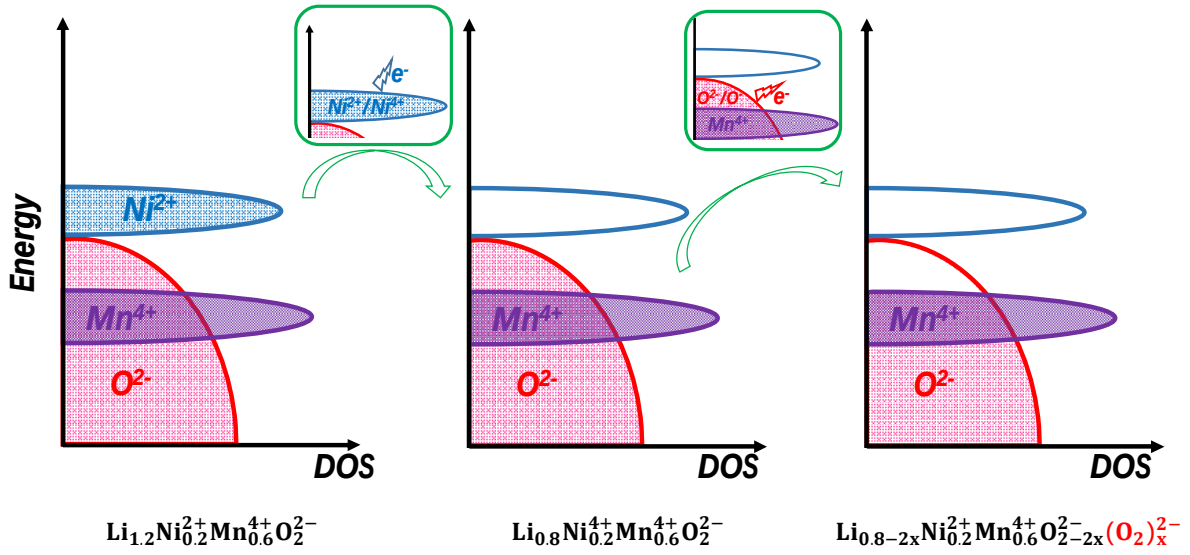

Figure S16. Schematic representation of the density of states (DOS) of $Li_{1.2}Ni_{0.2}Mn_{0.6}O_2$ during charge process.

Table S17. Crystallographic parameters obtained from the Rietveld refinement for the Li_2MnO_3 (C2/m) phase of $Li_{1.2}Ni_{0.2}Mn_{0.6}O_2$.

Li_2MO_3 (C2/m) Rwp=0.023 Rp=0.017						
a = 4.959Å, b = 8.284 Å c = 5.037Å β = 109.07°						
Atom	**site**	**x**	**y**	**z**	**Occ.$_{theo}$**	**Occ.$_{refined}$**
Mn	4g	0	0.165	0	0.9	0.9
Ni	4g	0	0.165	0	0.1	0.0948
Li	4g	0	0.165	0	0	0.0052
Ni	2c	0	0	0.5	0	0.0020
Li	2c	0	0	0.5	1	0.9980
Ni	4h	0	0.66	0.5	0	0.0036
Li	4h	0	0.66	0.5	1	0.9964
Li	2b	0	0.5	0	0.6	0.5988
Ni	2b	0	0.5	0	0.4	0.4012
O	4i	0.178	0	0.208	1	1
O	8j	0.253	0.320	0.231	1	1

Reference:

[1] J. Ye, Y. X. Li, L. Zhang, X. P. Zhang, M. Han, P. He, H. S. Zhou, *ACS Appl. Mater. Interfaces* **2016**, *8*, 208.

[2] Y. Qiao, S. Wu, J. Yi, Y. Sun, S. Guo, S. Yang, P. He, H. Zhou, *Angew. Chem. Int. Ed.* **2017**, *56*, 4960.

[3] J. F. Li, Y. F. Huang, Y. Ding, Z. L. Yang, S. B. Li, X. S. Zhou, F. R. Fan, W. Zhang, Z. Y. Zhou, Y. WuDe, B. Ren, Z. L. Wang, Z. Q. Tian, *Nature* **2010**, *464*, 392

[4] P. E. Blöchl, *Phys. Rev. B* **1994**, *50*, 17953.

[5] W. Kohn, L. J. Sham, *Phys. Rev.* **1965**, *140*, A1133.

[6] J. P. Perdew, K. Burke, M. Ernzerhof, *Phys. Rev. Lett.* **1996**, *77*, 3865.

[7] H. J. Monkhorst, J. D. Pack, *Phys. Rev. B* **1976**, *13*, 5188.

[8] a) N. Yabuuchi, K. Yoshii, S.-T. Myung, I. Nakai, S. Komaba, *J. Am. Chem. Soc.* **2011**, *133*, 4404; b) S. Hy, F. Felix, J. Rick, W. N. Su, B. J. Hwang, *J. Am. Chem. Soc.* **2014**, *136*, 999.

[9] a) E. McCalla, A. M. Abakumov, M. Saubanere, D. Foix, E. J. Berg, G. Rousse, M. L. Doublet, D. Gonbeau, P. Novak, G. Van Tendeloo, R. Dominko, J. M. Tarascon, *Science* **2015**, *350*, 1516; b) M. Sathiya, G. Rousse, K. Ramesha, C. P. Laisa, H. Vezin, M. T. Sougrati, M. L. Doublet, D. Foix, D. Gonbeau, W. Walker, A. S. Prakash, M. Ben Hassine, L. Dupont, J. M. Tarascon, *Nat. Mater.* **2013**, *12*, 827; c) M. Sathiya, A. M. Abakumov, D. Foix, G. Rousse, K. Ramesha, M. Saubanere, M. L. Doublet, H. Vezin, C. P. Laisa, A. S. Prakash, D. Gonbeau, G. VanTendeloo, J. M. Tarascon, *Nat. Mater.* **2015**, *14*, 230; d) P. E. Pearce, A. J. Perez, G. Rousse, M. Saubanère, D. Batuk, D. Foix, E. McCalla, A. M. Abakumov, G. Van Tendeloo, M.-L. Doublet, J.-M. Tarascon, *Nat. Mater.* **2017**, *16*, 580.

[10] a) J.-C. Dupin, D. Gonbeau, P. Vinatier, A. Levasseur, *Phys. Chem. Chem. Phys.* **2000**, *2*, 1319; b) L. Dahéron, R. Dedryvere, H. Martinez, M. Ménétrier, C. Denage, C. Delmas, D. Gonbeau, *Chem. Mater.* **2007**, *20*, 583.

[11] D. Aurbach, I. Weissman, A. Schechter, H. Cohen, *Langmuir* **1996**, *12*, 3991.

[12] J. S. Kim, C. S. Johnson, J. T. Vaughey, M. M. Thackeray, S. A. Hackney, *Chem. Mater.* **2004**, *16*, 1996.

[13] N. Twu, X. Li, A. Urban, M. Balasubramanian, J. Lee, L. Liu, G. Ceder, *Nano Lett.* **2014**, *15*, 596.

[14] H. R. Chen, M. S. Islam, *Chem. Mater.* **2016**, *28*, 6656.